High Density Reflection Spectroscopy I. A case study of GX 339-4

Jiachen Jiang,[1]* Andrew C. Fabian,[1] Jingyi Wang,[2] Dominic J. Walton,[1]
Javier A. García,[3,4] Michael L. Parker[5], James F. Steiner,[2] and John A. Tomsick[6]

[1]*Institute of Astronomy, University of Cambridge, Madingley Road, Cambridge CB3 0HA*
[2]*MIT Kavli Institute for Astrophysics and Space Research, MIT, 70 Vassar Street, Cambridge, MA 02139, USA*
[3]*Cahill Center for Astronomy and Astrophysics, California Institute of Technology, Pasadena, CA 91125, USA*
[4]*Dr. Karl Remeis-Observatory and Erlangen Centre for Astroparticle Physics, Sternwartstr. 7, D-96049 Bamberg, Germany*
[5]*European Space Agency (ESA), European Space Astronomy Centre (ESAC), E-28691 Villanueva de la Cañada, Spain*
[6]*Space Sciences Laboratory, 7 Gauss Way, University of California, Berkeley, CA 94720-7450, USA*

ABSTRACT

We present a broad band spectral analysis of the black hole binary GX 339-4 with *NuSTAR* and *Swift* using high density reflection model. The observations were taken when the source was in low flux hard states (LF) during the outbursts in 2013 and 2015, and in a very high flux soft state (HF) in 2015. The high density reflection model can explain its LF spectra with no requirement for an additional low temperature thermal component. This model enables us to constrain the density in the disc surface of GX 339-4 in different flux states. The disc density in the LF state is $\log(n_e/\text{cm}^{-3}) \approx 21$, 100 times higher than the density in the HF state ($\log(n_e/\text{cm}^{-3}) = 18.93^{+0.12}_{-0.16}$). A close-to-solar iron abundance is obtained by modelling the LF and HF broad band spectra with variable density reflection model ($Z_{\text{Fe}} = 1.50^{+0.12}_{-0.04} Z_\odot$ and $Z_{\text{Fe}} = 1.05^{+0.17}_{-0.15} Z_\odot$ respectively).

Key words: accretion, accretion discs - X-rays: binaries - X-rays: individual (GX 339-4)

1 INTRODUCTION

The primary X-ray spectra from black holes (BHs) can be described by a power-law continuum, which originates from a high temperature compact structure external to the black hole accretion disc. This high temperature compact structure is called the corona. The interaction between the primary power-law photons and the disc top layer can produce both emission, including fluorescence lines and recombination continuum, and absorption edges. These features are referred to as the disc reflection spectrum (e.g. George & Fabian 1991; García & Kallman 2010). The disc reflection spectrum is highly affected by relativistic effects, such as Doppler effect and gravitational redshift, due to the strong gravitational field in the vicinity of black holes (e.g. Reynolds & Nowak 2003). For example, relativistic blurred Fe Kα emission line features have been detected in reflection spectra of both Active Galactic Nuclei (AGN, e.g. MCG-6−30−15, Tanaka et al. 1995) and Galactic BH X-ray Bi-

nary sources (XRB, e.g. Cyg X-1, Barr et al. 1985). Relativistic reflection spectra can provide information on the disc-corona geometry, such as the coronal region size and the disc inner radius. By comparing relativistic reflection spectra in different observations, we can investigate changes of the inner accretion processes through the evolution of the X-ray flux states in both highly variable AGNs (e.g. Mrk 335, IRAS 13224−3809, Parker et al. 2014; Jiang et al. 2018) and XRBs that show different flux states (e.g. XTE J1650-500, Reis et al. 2013).

The existence of two different flux states in XRB was first realized in the X-ray emission of the XRB Cyg X-1 (Oda et al. 1971). Its X-ray spectrum can change from a soft spectrum featured by a strong thermal component to a hard spectrum featured by a strong disc reflection component. The soft state, which is also characterised by no radio detection, is identified as the 'high' flux (HF) state and the hard state with associated radio detection, is identified as the 'low' flux (LF) state, due to the large flux variation during the transition. Measurements in the HF soft states of BH XRB offer good evidence that the accretion disc is extended

* E-mail: jj447@cam.ac.uk

to the innermost stable circular orbit (ISCO, e.g. LMC X-3, Steiner et al. 2010). Most of the spin measurements of soft states are based on the assumption that the inner radius is located at ISCO (e.g. Gou et al. 2014; Walton et al. 2016). In the LF hard state, the disc is predicted to be truncated at a large radius and replaced by an advective flow at small radii (Esin et al. 1997; Narayan 2005). Although there is evidence that the disc is truncated as measured by reflection spectroscopy at X-ray luminosities $L_{\rm X} \approx 0.1\% L_{\rm Edd}$ (Tomsick et al. 2009; Narayan & McClintock 2008), there is a substantial debate whether the disc is truncated in the intermediate flux hard state due to different spectral modelling or instrumental pile-up effects (see the discussion in Wang-Ji et al. 2018).

A common result obtained by reflection modelling of black hole X-ray spectra is high iron abundance compared to solar. For example, Walton et al. (2016) found a value of $Z_{\rm Fe} \approx 4 Z_\odot$ in Cyg X-1 and Parker et al. (2015) obtained $Z_{\rm Fe} \approx 4.7 Z_\odot$ in the same source. Similarly, an iron abundance of $Z_{\rm Fe} \approx 2 - 5 Z_\odot$ is required for another BH XRB V404 Cyg (Walton et al. 2017). Such a high iron abundance has been commonly seen in AGNs as well (e.g. Chiang et al. 2015; Parker et al. 2018). Wang et al. (2012) found that the metallicty of the outflows in different quasars can vary between 1.7–6.9$Z_\odot$. Reynolds et al. (2012) suggested that the radiation-pressure dominance of the inner disc may enhance the iron abundances. However radiative levitation effects make predictions for a change of the inner disc iron abundance, which is difficult to be observed in AGNs due to their longer dynamical timescales.

Another possible explanation for the high iron abundances is high density reflection. Most versions of available disc reflection models assume a constant electron density $n_{\rm e} = 10^{15} {\rm cm}^{-3}$ for the top layer of the BH accretion disc, which is appropriate for very massive supermassive black holes in AGNs (e.g. $M_{\rm BH} > 10^8 M_\odot$). For example, an upper limit of $n_{\rm e} < 10^{15.3} {\rm cm}^{-3}$ is obtained in Seyfert 1 galaxy 1H0419−577 ($M_{\rm BH} \approx 1.3 \times 10^8 M_\odot$, Grupe et al. 2010) by fitting its *XMM-Newton* spectra with variable density reflection model (Jiang submitted). At higher electron density, the free-free process becomes more important in constraining low energy photons, increasing the temperature of the top layer of the disc, and thus turning the reflected emissions below 1 keV into a blackbody shaped spectrum (Ross & Fabian 2007; García et al. 2016). Such a model can potentially relieve the very high iron abundance required in previous reflection spectral modelling. For instance, Tomsick et al. (2018) obtained an electron density of $n_{\rm e} \approx 3 \times 10^{20} {\rm cm}^{-3}$ by fitting the Cyg X-1 intermediate flux state spectra with the high electron density reflection model. Although the iron abundance was fixed at the solar value during the spectral fitting, the model successfully explains the spectra. Jiang et al. (2018) fitted the narrow line Seyfert 1 galaxy IRAS 13224−3809 spectra and obtained an electron density of $n_{\rm e} > 10^{19.7} {\rm cm}^{-3}$ with an iron abundance of $Z_{\rm Fe} \approx 5 Z_\odot$, which is significantly lower than the previous results $Z_{\rm Fe} \approx 20 Z_\odot$ and closer to the iron abundance measured in the ultra-fast outflow of the same source.

Higher densities may also potentially explain the weak low temperature thermal component found in the LF state of the XRBs (e.g. Reis et al. 2008; Wang-Ji et al. 2018) and at least some of the soft excess commonly seen in Seyfert

galaxies (e.g. Fabian et al. 2009; Chiang et al. 2015; Jiang et al. 2018). The inclusion of the high electron density effects significantly decreases the flux of the best-fit blackbody component in IRAS 13224−3809 required for the spectral fitting purpose (Jiang et al. 2018). It is also interesting to note that the best-fit flux and temperature of the blackbody component that accounts for the soft excess in IRAS 13224−3809 show a $F \propto T^4$ relation, indicating a constant area origin of the soft excess emission (Chiang et al. 2015; Jiang et al. 2018).

GX 339-4 is a low mass X-ray binary (LMXB) and shows activity in a wide range of wavelength from optical to X-ray. The mass of the central black hole still remains uncertain. For example, Heida et al. (2017) obtained a black hole mass of $2 - 10 M_\odot$ by studying its near infrared spectrum and a mass of $> 5 M_\odot$ is obtained previously by Hynes et al. (2003a,b); Muñoz-Darias et al. (2008). The distance has been estimated to be $\approx 7 {\rm kpc}$ (Zdziarski et al. 2004). GX 339−4 has shown frequent outbursts and multiple X-ray observations have been taken during different spectral states of GX 339-4. In its hard state, its X-ray spectrum shows a broad iron emission line and a power-law continuum with a photon index varying between $\Gamma \approx 1.5 - 2.5$ across different flux levels (Miller et al. 2004, 2006, 2008). Reis et al. (2008) presented a systematic study of its high and low hard state *XMM-Newton* and *RXTE* spectra by taking the blackbody radiation from the disc into the top layer as well as the Comptonization effects into modelling, and obtained a black hole spin of $a_* = 0.94 \pm 0.02$. More recently, Parker et al. (2016) obtained a disc iron abundance of $Z_{\rm Fe} \approx 6.6 Z_\odot$ for the HF soft state *NuSTAR* and *Swift* spectra of GX 339-4. In this study, the disc inner radius is assumed to be located at ISCO and a black hole spin of $a_* > 0.95$ is obtained by combining disc thermal spectral and reflection spectral modelling. Later, Wang-Ji et al. (2018) found $Z_{\rm Fe} \approx 8 Z_\odot$ for the LF state of the same source observed by the same instruments. Similar conclusions were found by analysing its stacked *RXTE* spectra at the LF states (García et al. 2015) and *NuSTAR* spectra during the outburst of 2013 (Fürst et al. 2015).

In this paper, we present a high density reflection interpretation of both LF and HF state spectra of GX 339-4. The same *NuSTAR* and *Swift* spectra as in Parker et al. (2016); Wang-Ji et al. (2018) are considered. In Section 2, we introduce the data reduction process; in Section 3, we introduce the details of high density reflection modelling of the LF and HF spectra of GX 339-4; in Section 4, we present and discuss the final spectral fitting results. The high density reflection modelling of AGN spectra are presented in a companion paper (Jiang in prep).

2 OBSERVATIONS AND DATA REDUCTION

The weekly *MAXI* hardness-intensity diagram (HID) for the 2009-2018 period of GX 339-4 (Matsuoka et al. 2009) is shown in Fig. 1, showing a standard 'q-shaped' behaviour during the outbursts. GX 339-4 went through two outbursts each in 2013 and 2015. 11 *NuSTAR* observations in total, each with a corresponding *Swift* snapshot, were triggered during these two outbursts, shown by the arrow in Fig. 1. The *NuSTAR* LF observations in 2015 were taken only dur-

Table 1. *NuSTAR* and *Swift* observations of GX 339-4 in 2013 and 2015. WT: window timing mode; PC: photon counting mode.

Obs	*NuSTAR* obsID	Date	exp.(ks)	*Swift* obsID	Date	exp.(ks)	Mode
HF	80001015003	2015-03-04	30.9	00081429002	2015-03-04	1.9	WT
LF1	80102011002	2015-08-28	21.6	00032898124	2015-08-29	1.7	WT
LF2	80102011004	2015-09-02	18.3	00032898126	2015-09-03	2.3	WT
LF3	80102011006	2015-09-07	19.8	00032898130	2015-09-07	2.8	WT
LF4	80102011008	2015-09-12	21.5	00081534001	2015-09-12	2.0	PC
LF5	80102011010	2015-09-17	38.5	00032898138	2015-09-17	2.3	WT
LF6	80102011012	2015-09-30	41.3	00081534005	2015-09-30	2.0	PC
LF7	80001013002	2013-08-11	42.3	00032490015	2013-08-12	1.1	WT
LF8	80001013004	2013-08-16	47.4	00080180001	2013-08-16	1.9	WT
LF9	80001013006	2013-08-24	43.4	00080180002	2013-08-24	1.6	WT
LF10	80001013008	2013-09-03	61.9	00032898013	2013-09-02	2.0	WT
LF11	80001013010	2013-10-16	98.2	00032988001	2013-10-17	9.6	WT
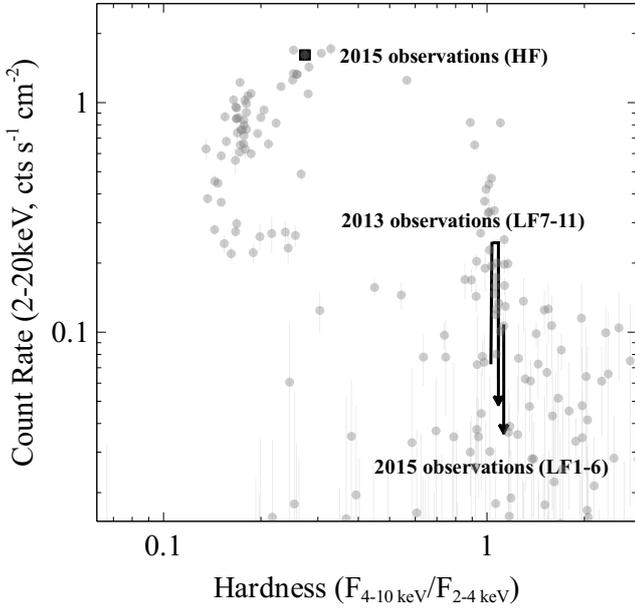
Figure 1. Weekly *MAXI* hardness-intensity diagram for the 2009-2018 period of GX 339-4. The black square and the arrows correspond to the dates of the HF observations and the LF(1-11) observations analysed in this work. The arrows show the flux change during the *NuSTAR* monitoring of the outbursts. *NuSTAR* observations were taken during the rise and decay of the outburst in 2013, and only during the decay of the outburst in 2015.

ing the decay of the outburst. In this work, we consider all of the *NuSTAR* observations taken during these two outbursts. In March 2015, GX 339-4 was detected with strong thermal and power-law components by *Swift*, suggesting strong evidence of a HF state with a combination of disc thermal component and reflection component. One *NuSTAR* target of opportunity observation was triggered with a simultaneous *Swift* snapshot. See the black square in Fig. 1 for the flux and hardness state of the source during its HF observations. A full list of observations are shown in Table 1.

2.1 *NuSTAR* Data Reduction

The standard pipeline NUPIPELINE V0.4.6, part of HEA-SOFT V6.23 package, is used to reduce the *NuSTAR* data. The *NuSTAR* calibration version V20171002 is used. We extract source spectra from circular regions with radii of 100 arcsec, and the background spectra from nearby circular regions on the same chip. The task NUPRODUCTS is used for this purpose. The 3-78 keV band is considered for both FPMA and FPMB spectra. The spectra are grouped to have a minimum signal-to-noise (S/N) of 6 and to oversample by a factor of 3.

2.2 *Swift* Data Reduction

The *Swift* observations are processed using the standard pipeline XRTPIPELINE V0.13.3. The calibration file version used is x20171113. The LF observations taken in the WT mode are not affected by the pile-up effects. The source spectra are extracted from a circular region with a radius of 20 pixels [1] and the background spectrum spectra are extracted from an annular region with an inner radius of 90 pixels and an outer radius of 100 pixels. The LF observations taken in the PC mode are affected by the pile-up effects. By following Wang-Ji et al. (2018) where they estimated the PSF file, a circular region with a radius of 5 pixels is excluded in the center of the source region. The 0.6–6 keV band of all the LF *Swift* XRT spectra are considered. The HF observation was taken in the WT mode and was affected by pile-up effects. By following Parker et al. (2016), a circular radius of 10 pixels is excluded in the center of the source region. The 0.6–1 keV of the HF *Swift* XRT spectrum at a very high flux state is ignored due to known issues of the RMF redistribution issues in the WT mode [2]. The *Swift* XRT spectra are grouped to have a minimum S/N of 6 and to oversample by a factor of 3.

---

[1] 1 pixel ≈ 2.36″

[2] See following website for more XRT WT mode calibration information. http://www.swift.ac.uk/analysis/xrt/digest_cal.php

3   SPECTRAL ANALYSIS

XSPEC V12.10.0.C (Arnaud 1996) is used for spectral analysis, and C-stat is considered in this work. The Galactic column density towards GX 339-4 remains uncertain. The value of combined $N_{\mathrm{H_I}}$ and $N_{\mathrm{H_2}}$ obtained by Willingale et al. (2013) is $5.18 \times 10^{21} \mathrm{cm}^{-2}$. However, Kalberla et al. (2005) reported a column density of $3.74 \times 10^{21} \mathrm{cm}^{-2}$ in the Leiden/Argentine/Bonn survey. The Galactic column density values measured by different sets of broad band X-ray spectra are different too. For example, Wang-Ji et al. (2018) obtained $\approx 4 \times 10^{21} \mathrm{cm}^{-2}$ while Parker et al. (2016) obtained a higher value of $7.7 \pm 0.2 \times 10^{21} \mathrm{cm}^{-2}$. We therefore fixed the Galactic column density at $3.74 \times 10^{21} \mathrm{cm}^{-2}$ in the beginning of our analysis and allow it to vary to obtain the best-fit value for each set of spectra. For local Galactic absorption, the `tbabs` model is used. The solar abundances of Wilms et al. (2000) are used in `tbabs`. An additional constant model `constant` has been applied to vary normalizations between the simultaneous spectra obtained by different instruments to account for calibration uncertainties.

### 3.1   Low Flux State (LF) Spectral Modelling

We analyze all the LF *NuSTAR* observations publicly available prior to 2018 and they have discussed in Fürst et al. (2015); Wang-Ji et al. (2018). Fig. 2 shows the ratio plots of LF1-11 spectra fitted with a Galactic absorbed power-law model obtained by fitting only the corresponding *NuSTAR* spectra. All the LF spectra show a broad emission line feature around 6.4 keV with a Compton hump above 20 keV. They provide a strong evidence of a relativistic disc reflection component. By following García et al. (2015); Wang-Ji et al. (2018), we model the features with a combination of relativistic disc reflection and a distant reflector for the narrow emission line component. A more developed version of `reflionx` (Ross & Fabian 2005) is used to model the rest-frame disc reflection spectrum. The `reflionx` grid allows the following free parameters: disc iron abundance (Z_{Fe}), disc ionization $\log(\xi)$, disc electron density n_{e}, high energy cutoff (E_{cut}), and photon index (Γ). All the other element abundances are fixed at the solar value (Morrison & McCammon 1983). The ionization parameter is defined as $\xi = 4\pi F / n$, where F is the total illuminating flux and n is the hydrogen number density. The photon index Γ and high energy cutoff E_{cut} are linked to the corresponding parameters of the coronal emission modelled by `cutoffpl` in XSPEC. A convolution model `relconv` (Dauser et al. 2013) is applied to the rest frame ionized disc reflection model `reflionx` to apply relativistic effects. A simple power-law shaped emissivity profile is assumed ($\epsilon \propto r^{-q}$) and the emissvity index q is allowed to vary during the fit. Other free parameters are the disc viewing angle i and the disc inner radius $r_{\mathrm{in}}/\mathrm{ISCO}$. The ionization of the distant reflector is fixed at the minimum value $\xi = 10$. The other parameters of the distant reflector are linked to the corresponding parameters in the disc reflection component. The BH spin parameter a_* is fixed at its maximum value 0.998 (Kerr 1963) to fully explore the r_{in} parameter. We use `cflux`, a simple convolution model in XSPEC, to calculate the 1–10 keV flux of each model component. For future reference and simplicity, we define an empirical reflection fraction as $f_{\mathrm{refl}} = F_{\mathrm{ref}}/F_{\mathrm{pl}}$ in the 1–

10 keV band, where F_{ref} and F_{pl} are the flux of the disc reflection component and the coronal emission calculated by `cflux`. Note that this is not the same as the physically defined reflection fraction discussed by Dauser et al. (2016). The final model is `tbabs * ( cflux*(relconv*reflionx) + cflux*reflionx + cflux*cutoffpl)` in XSPEC format. This model can fit all LF spectra successfully with no obvious residuals. For example, it offers a good fit for the LF1 spectra with C-stat/ν = 1043.52/948. A ratio plot of LF1 spectra fitted with this model is shown in the top panel of Fig. 3. The best-fit values of some key parameters that affect the spectral modelling below 3 keV are following: $N_{\mathrm{H}} = 3.4^{+0.2}_{-0.1} \times 10^{21}$ cm^{-2}, $\log(\xi/\mathrm{erg\ cm\ s^{-1}}) = 3.18^{+0.07}_{-0.06}$, and $\log(n_{\mathrm{e}}/\mathrm{cm}^{-3}) = 20.6 \pm 0.3$. Our best-fit column density is consistent with the Galactic column density measured in Kalberla et al. (2005).

We notice that previously the spectral modelling requires a low temperature multicolour disc thermal component `diskbb` ($kT = 0.46\,\mathrm{keV}$) when using the model with the disc electron density n_{e} fixed at $\log(n_{\mathrm{e}}/\mathrm{cm}^{-3}) = 15$ for LF1 observation (Wang-Ji et al. 2018). However the normalization of this component is very low and weakly constrained. Similarly, a weak thermal component is also required in the analysis of its *XMM-Newton* hard state observations (Reis et al. 2008) and other earlier *NuSTAR* observations (Reis et al. 2013). The difference in spectral modelling may result from the following two reasons: one is the high density reflection model, where a blackbody-shaped emission arises in the soft band when the disc electron density n_{e} becomes higher than 10^{15} cm^{-3}; the other is the uncertain neutral absorber column density, which was measured to be $N_{\mathrm{H}} = 4.12^{+0.08}_{-0.12} \times 10^{21}$ cm^{-2} in Wang-Ji et al. (2018) and higher than our best-fit value for the LF1 spectra.

In order to test for an additional `diskbb` component, we first fit the spectra with N_{H} fixed at the higher Galactic column density $N_{\mathrm{H}} = 5.18 \times 10^{21}$ cm^{-2} obtained by Willingale et al. (2013) rather than the value from Kalberla et al. (2005). An additional `diskbb` component improves the fit by only ΔC-stat=1.1. See the middle panel of Fig. 3 for the corresponding ratio plot. Only an upper limit of the `diskbb` normalization is of $N_{\mathrm{diskbb}} < 1.5 \times 10^5$ found. Compared with the result in Wang-Ji et al. (2018), a lower disc inner temperature of $kT = 0.24^{+0.08}_{-0.10}$ keV is required in this fit. Second, we fit LF1 spectra with the absorber column density as a free parameter (bottom panel of Fig 3). A contour plot of C-stat distribution on the N_{H} vs. N_{diskbb} parameter plane is calculated by STEPPAR function in XSPEC and shown in Fig. 4. It clearly shows a strong degeneracy between the absorber column density and the normalization of the `diskbb` component. The fit is only improved by ΔC-stat=3 with 2 more free parameters after including this `diskbb` component. See Fig. 3 for ratio plots against different continuum models. By varying the Galactic column density, it only slightly changes the fit of the *Swift* XRT spectrum. Therefore, we conclude that an additional `diskbb` component is not necessary for LF1 spectral modelling when the disc density parameter n_{e} is allowed to vary. In order to visualize the spectral difference with different n_{e}, we show the best-fit reflection model component for LF1 in Fig. 5 in comparison with the best-fit model for the same observation assuming $\log(n_{\mathrm{e}}/\mathrm{cm}^{-3}) = 15$ cm^{-3} in Wang-Ji et al. (2018). With a disc
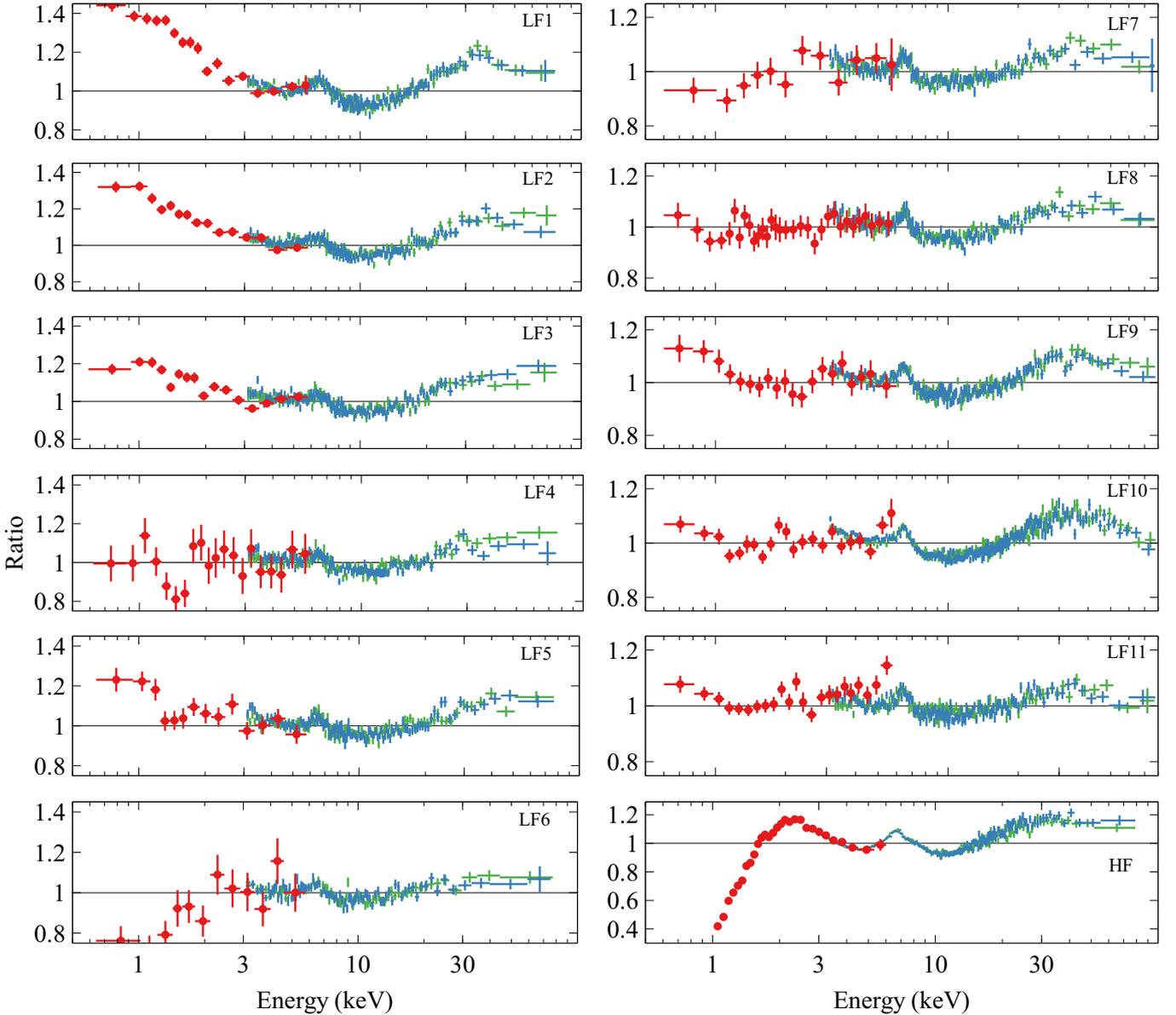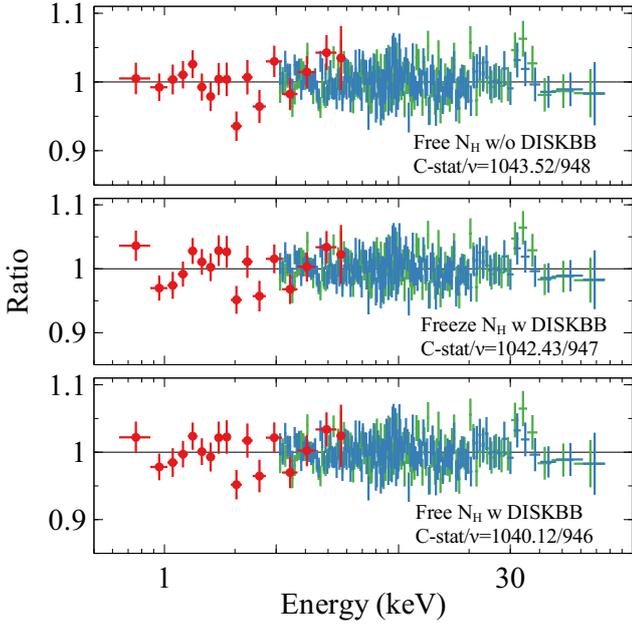
Figure 2. First 11 panels: ratio plots of GX 339-4 FPM (blue crosses: FPMA; green crosses: FPMB) and XRT (red circles) spectra fitted with a Galactic absorbed power law for LF observations in 2015 (LF1-6) and 2013 (LF7-11). Last panel: ratio plot of HF spectra fitted with a Galactic absorbed power law plus a simple blackbody component for the very high flux soft state observation in 2015. All the spectra show a broad line emission feature around 6.4 keV and a strong Compton hump above 10 keV.
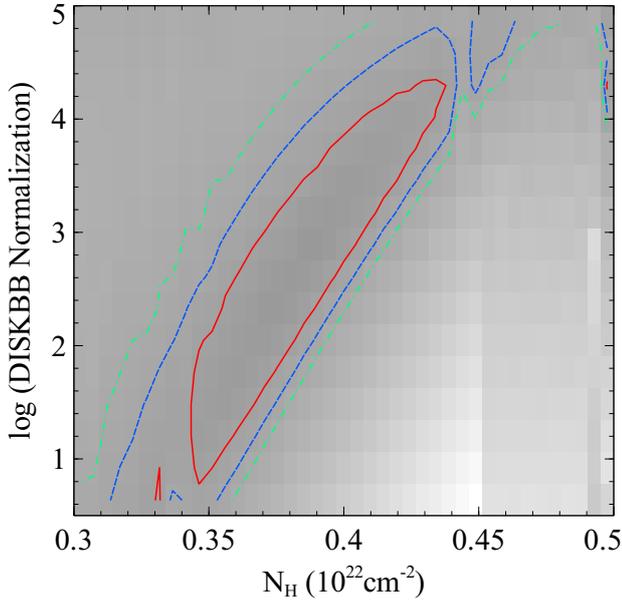
density as high as $\log(n_e/\mathrm{cm}^{-3}) = 20.6$, a quasi-blackbody emission arises in the soft band and accounts for the excess emission below 2 keV. Similar conclusions are found for the other sets of LF spectra. Future pile-up free high S/N observation below 2 keV, such as from *NICER*, may help constrain more detailed spectral shape of LF states of GX 339-4.

So far we have achieved the best-fit model for the LF spectra individually. We also undertake a multi-epoch spectral analysis with disc iron abundance Z_{Fe} and disc viewing angle i linked between LF1-11 spectra. All the other parameters are allowed to vary during the fit. A table of all the best-fit parameters are shown in Table. 2. The best-fit models and corresponding ratio plots are shown in Fig. 6. We allow the column density of the neutral absorber to vary in
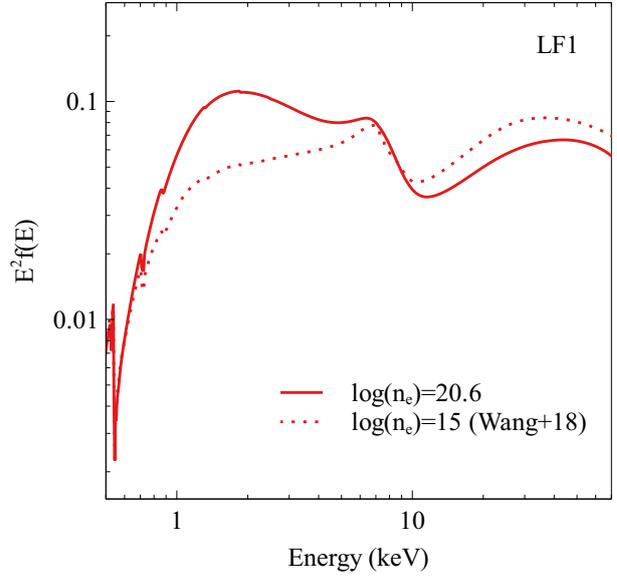
different epochs to investigate any variance. A slightly higher column density ($N_{\mathrm{H}} \approx 4.1 \times 10^{21}\,\mathrm{cm}^{-2}$) is required for LF6,7. The emissivity index of the relativistic reflection spectrum is weakly constrained in LF3-6 observations but largely consistent with the Newtonian value $q = 3$, except for the LF1 observation. We can also confirm that the disc is not truncated at a significantly large radius, such as $r = 100r_g$ (Plant et al. 2015). A slight iron over abundance compared to solar is required ($Z_{\mathrm{Fe}} = 1.5^{+0.12}_{-0.04}$) for the spectral fitting. The power-law continuum is softer in the first two observations taken at higher flux levels but remains consistent at 90% confidence during the rest of the decay in 2015. The photon index in LF7-10 during the outburst in 2013 is consistent at 90% confidence as well. The reflection fraction decreases

Figure 3. Ratio plots for LF1 spectra against different continuum models. Red circles: XRT; blue crosses: FPMA; green crosses: FPMB. See text for more details.
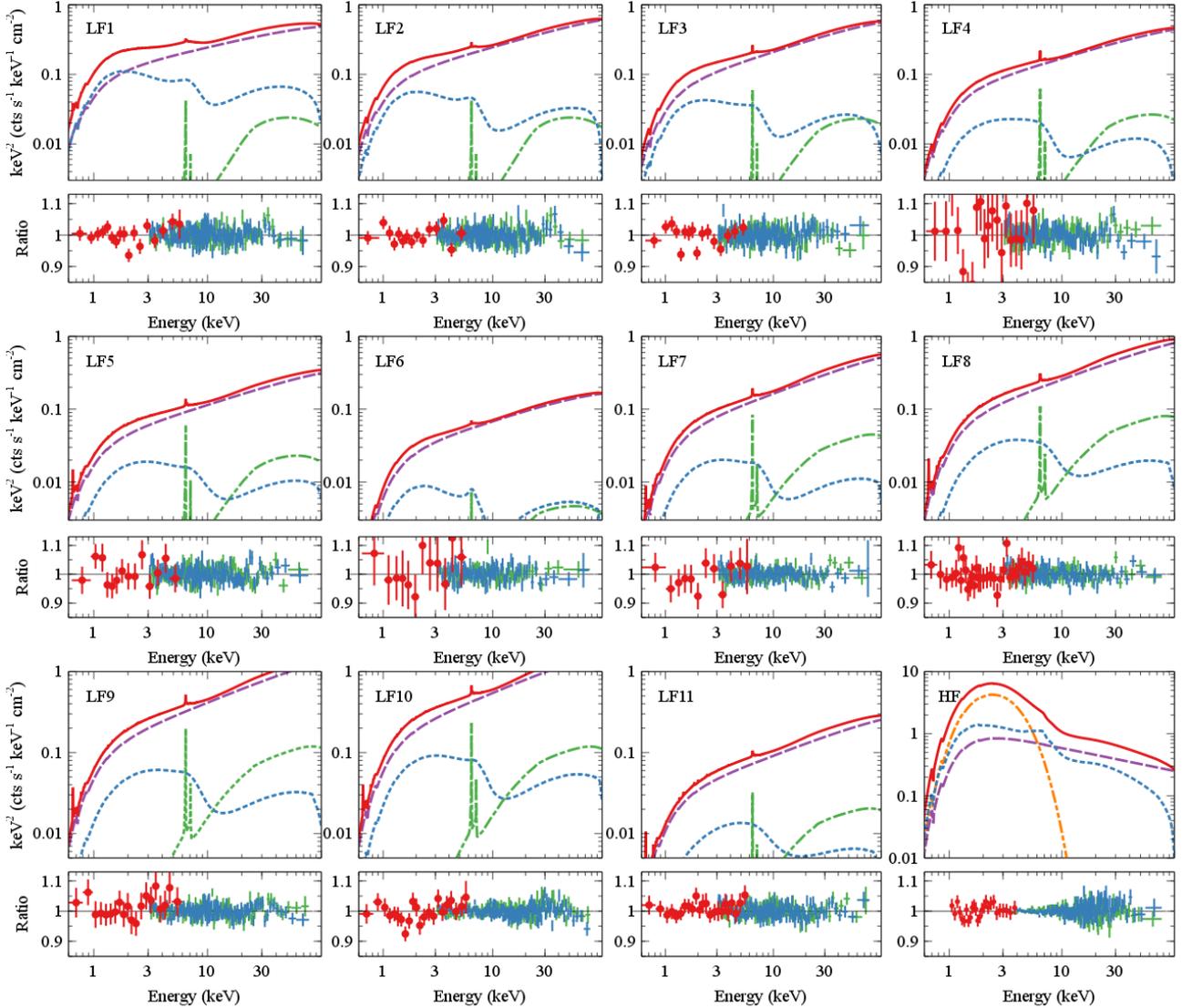

Figure 5. The best-fit relativistic high density reflection model for LF1 spectra (solid line) and the best-fit relativistic reflection model obtained by Wang-Ji et al. (2018) assuming $\log(n_e/\mathrm{cm}^{-3}) = 15$ (dotted line). The plot is only shown for comparison of spectral shape. An additional `diskbb` component is required to fit the broad band spectra in Wang-Ji et al. (2018).

with the decreasing total flux during the flux decay in 2015. This is likely caused by a receding inner disc radius at the very low flux states or a change of the coronal geometry (e.g. its height above the disc). Moreover, the multi-epoch spectral analysis of all LF observations shows tentative evidence for an anti-correlation between disc density and X-ray band flux. For example, the disc density increases from $\log(n_e/\mathrm{cm}^{-3}) = 20.60^{+0.23}_{-0.12}$ in the highest flux state (LF1) to $\log(n_e/\mathrm{cm}^{-3}) = 21.45^{+0.06}_{-0.13}$ in the lowest flux state (LF6). The flux level of the cold reflection component remains consistent, indicating that this emission arises from stable material at a large radius from the central black hole. We will discuss other fitting results, such as the electron density measurements, in Section 4.

3.2 High Flux State (HF) Spectral Modelling

The same *NuSTAR* and *Swift* observations of GX 339-4 in a HF state analysed in Parker et al. (2016) are considered here. A ratio plot of the HF spectra fitted with a Galactic absorbed power-law model and a simple disc blackbody component `diskbb` is shown in the bottom panel of Fig. 2. The HF spectra show a broad emission line feature at the iron band and a Compton hump above 10 keV, indicating existence of a relativistic disc reflection component similar with all the LF spectra. A multicolour disc blackbody component `diskbb` is used to account for the strong disc thermal component. The full model is `tbabs * ( cflux*(relconv*reflionx) + cflux*reflionx + cflux*cutoffpl + diskbb)` in XSPEC format. This model provides a good fit with C-stat/ν=1048.68/971. The best-fit model is shown in the last panel of Fig. 6 and the best-fit parameters are shown in the last column of Table 2. A disc density of $\log(n_e/\mathrm{cm}^{-3}) =$

Figure 4. A contour plot of C-stat distribution on the Galactic absorption column density N_H vs. `diskbb` model normalization parameter plane for LF1 spectra when fitted with `tbabs*(diskbb+cutoffpl+relconv*reflionx+reflionx)`. It shows a clear degeneracy between two parameters. The lines show the 1σ (red solid line), 2σ (blue dashed line), and 3σ contours (green dash-dot line).

Figure 6. Top: the first 11 panels show the best-fit models obtained by fitting LF1-11 spectra simultaneously. The last panel shows the best-fit model obtained by fitting only HF spectra. Red solid lines: total model; blue dotted lines: relativistic reflection model; purple dashed lines: coronal emission; green dash-dot lines: distant reflection component; orange dash-dot-dot lines: disc thermal spectrum (only needed in the HF spectral modelling). Bottom: ratio plots against the corresponding best-fit models shown in the upper panels. Red circles: XRT; blue crosses: FPMA; green crosses: FPMB.

$18.93^{+0.12}_{-0.16}$ is found in HF observations which is 100 times lower than the best-fit value in LF observations.

So far we have obtained a good fit for the HF spectrum of GX 339-4. A higher column density is required for the neutral absorber ($N_{\mathrm{H}} = 6.2 \pm 0.2 \times 10^{21}$ cm^{-2}) compared to the LF observations ($N_{\mathrm{H}} \approx 3.4 \times 10^{21}$ cm^{-2}). Parker et al. (2016) obtained a higher column density of $N_{\mathrm{H}} = 7.2 \pm 0.2 \times 10^{21}$ cm^{-2} for the same observation assuming $n_{\mathrm{e}} = 10^{15}$ cm^{-3} for the disc. Both our result and Parker et al. (2016) are higher than the Galactic absorption column density estimated at other wavelengths (e.g. Kalberla et al. 2005), indicating a possible extra variable neutral absorber along the line of sight. Only an upper limit of the flux of the distant cold reflector is achieved ($\log(F_{\mathrm{dis}}) < -10.89$). The 1–10 keV band flux values of the disc reflection component and the coronal emission increase by a factor of 13 and 6 respectively compared

to LF1. The best-fit broad band model shows the highest reflection fraction among all the observations considered in this work, indicating a geometry change of the disc corona system such as a small inner disc radius. A solar iron abundance ($1.05^{+0.17}_{-0.15}$) is required for the HF spectra, which is lower than the value obtained by Parker et al. (2016), where a disc density of $n_{\mathrm{e}} = 10^{15}$ cm^{-3} is assumed.

4 RESULTS AND DISCUSSION

We have obtained a good fit for the LF and the HF pectra of GX 339-4. The LF spectral modelling requires a high disc density of $\log(n_{\mathrm{e}}/\mathrm{cm}^{-3}) \approx 21$ with no additional low temperature thermal component. The HF spectral modelling requires a 100 times lower density ($\log(n_{\mathrm{e}}/\mathrm{cm}^{-3}) = 18.93^{+0.12}_{-0.16}$)

Table 2. The best-fit parameters obtained by fitting 1) LF1-11 spectra simultaneously 2) only HF spectra. u: unconstrained; l: linked; f: fixed. $F_{\rm refl}$ is the flux of the relativistic disc reflection component measured between 1–10 keV; $F_{\rm pl}$ is the flux of the coronal emission measured at the same energy band; $F_{\rm dis}$ is for the distant cold reflector. The reflection fraction $f_{\rm refl}$ is defined as $F_{\rm refl}/F_{\rm pl}$ for simplicity. $L_{0.1-100\rm keV}$ is the 0.1–100 keV band Galactic-absorption corrected luminosity calculated using the best-fit model. A black hole mass $M_{\rm BH} = 10 M_\odot$ and a distance $d = 10\,\rm kpc$ are assumed.

Parameter	Unit	LF1	LF2	LF3	LF4	LF5	LF6
$N_{\rm H}$	$10^{21}\rm cm^{-2}$	$3.22^{+0.14}_{-0.08}$	$3.20^{+0.10}_{-0.12}$	$3.1^{+0.3}_{-0.2}$	$3.4^{+0.5}_{-0.5}$	$3.2^{+0.2}_{-0.3}$	$4.1^{+0.8}_{-0.7}$
q	-	6^{+3}_{-2}	$2.5^{+3.6}_{-0.4}$	< 7	$5({\rm u})$	$6({\rm u})$	$4({\rm u})$
rin	ISCO	<4.7	<8	<11	11^{+4}_{-7}	< 32	21^{+14}_{-12}
$\log(\xi)$	$\rm erg\,cm\,s^{-1}$	$3.18^{+0.06}_{-0.39}$	$3.13^{+0.12}_{-0.08}$	$3.12^{+0.09}_{-0.17}$	$3.10^{+0.17}_{-0.04}$	$3.12^{+0.11}_{-0.08}$	$3.08^{+0.05}_{-0.02}$
$\log(n_{\rm e})$	$\rm cm^{-3}$	$20.60^{+0.23}_{-0.12}$	$20.64^{+0.16}_{-0.13}$	$21.1^{+0.4}_{-0.2}$	$21.49^{+0.14}_{-0.13}$	$20.82^{+0.31}_{-0.15}$	$21.45^{+0.06}_{-0.13}$
a_*	-	$0.998({\rm f})$	(l)	(l)	(l)	(l)	(l)
i	deg	34 ± 2	(l)	(l)	(l)	(l)	(l)
$Z_{\rm Fe}$	$Z_\odot$	$1.50^{+0.12}_{-0.04}$	(l)	(l)	(l)	(l)	(l)
$\log(F_{\rm refl})$	$\rm erg\,cm^{-2}\,s^{-1}$	$-9.42^{+0.04}_{-0.09}$	$-9.72^{+0.07}_{-0.03}$	$-9.91^{+0.13}_{-0.05}$	$-10.13^{+0.11}_{-0.09}$	$-10.21^{+0.03}_{-0.06}$	$-10.53^{+0.10}_{-0.11}$
$E_{\rm cut}$	keV	350^{+92}_{-124}	>287	>255	>290	>350	>420
Γ	-	$1.594^{+0.004}_{-0.010}$	$1.530^{+0.018}_{-0.045}$	$1.49^{+0.02}_{-0.05}$	$1.517^{+0.010}_{-0.030}$	$1.485^{+0.007}_{-0.029}$	$1.49^{+0.03}_{-0.02}$
$\log(F_{\rm pl})$	$\rm erg\,cm^{-2}\,s^{-1}$	$-9.22^{+0.05}_{-0.03}$	-9.25 ± 0.03	$-9.32^{+0.02}_{-0.03}$	$-9.420^{+0.011}_{-0.028}$	$-9.601^{+0.009}_{-0.013}$	-9.82 ± 0.02
kT	keV	-	-	-	-	-	-
$N_{\rm diskbb}$	-	-	-	-	-	-	-
$f_{\rm refl}$	-	$0.631^{+0.010}_{-0.016}$	$0.3388^{+0.0041}_{-0.0010}$	$0.224^{+0.006}_{-0.002}$	$0.195^{+0.003}_{-0.002}$	$0.246^{+0.003}_{-0.002}$	$0.194^{+0.003}_{-0.002}$
$\log(F_{\rm dis})$	$\rm erg\,cm^{-2}\,s^{-1}$	$-11.01^{+0.16}_{-0.20}$	$-11.58^{+0.16}_{-0.31}$	$-11.40^{+0.19}_{-0.33}$	$-11.4^{+0.2}_{-0.3}$	$-11.16^{+0.15}_{-0.20}$	<-11.69
C-stat/ν		11870.25/11305					
$L_{0.1-100\rm keV}/L_{\rm Edd}$	%	2.7	2.5	2.2	1.7	1.2	0.6

Continued

Parameter	Unit	LF7	LF8	LF9	LF10	LF11	HF
$N_{\rm H}$	$10^{21}\rm cm^{-2}$	$4.1^{+0.3}_{-0.2}$	$3.84^{+0.18}_{-0.16}$	$3.41^{+0.18}_{-0.17}$	$3.71^{+0.16}_{-0.23}$	$3.75^{+0.12}_{-0.14}$	6.2 ± 0.2
q	-	> 0.5	> 2	>3	>2.7	$4({\rm u})$	$5.88^{+1.01}_{-0.77}$
rin	ISCO	<25	<17	<10	<1.51	<25	$1({\rm f})$
$\log(\xi)$	$\rm erg\,cm\,s^{-1}$	$3.29^{+0.04}_{-0.03}$	3.26 ± 0.03	$3.23^{+0.016}_{-0.020}$	$3.23^{+0.02}_{-0.05}$	$3.26^{+0.04}_{-0.03}$	$3.88^{+0.08}_{-0.12}$
$\log(n_{\rm e})$	$\rm cm^{-3}$	21.0 ± 0.2	$21.25^{+0.23}_{-0.17}$	21.15 ± 0.15	$20.93^{+0.12}_{-0.08}$	$21.57^{+0.20}_{-0.17}$	$18.93^{+0.12}_{-0.16}$
a_*	-	(l)	(l)	(l)	(l)	(l)	>0.93
i	deg	(l)	(l)	(l)	(l)	(l)	$35.9^{+1.6}_{-2.0}$
$Z_{\rm Fe}$	$Z_\odot$	(l)	(l)	(l)	(l)	(l)	$1.05^{+0.17}_{-0.15}$
$\log(F_{\rm refl})$	$\rm erg\,cm^{-2}\,s^{-1}$	$-10.071^{+0.009}_{-0.010}$	-9.93 ± 0.04	$-9.71^{+0.03}_{-0.02}$	$-9.52^{+0.03}_{-0.04}$	$-10.41^{+0.02}_{-0.07}$	$-8.30^{+0.03}_{-0.02}$
$E_{\rm cut}$	keV	>380	>320	>430	>330	>410	$500({\rm f})$
Γ	-	$1.427^{+0.065}_{-0.016}$	$1.419^{+0.012}_{-0.010}$	$1.421^{+0.009}_{-0.015}$	1.42 ± 0.02	$1.478^{+0.011}_{-0.018}$	$2.357^{+0.019}_{-0.018}$
$\log(F_{\rm pl})$	$\rm erg\,cm^{-2}\,s^{-1}$	$-9.467^{+0.007}_{-0.008}$	$-9.278^{+0.011}_{-0.013}$	$-9.068^{+0.010}_{-0.021}$	$-8.94^{+0.009}_{-0.008}$	$-9.701^{+0.015}_{-0.014}$	$-8.46^{+0.06}_{-0.05}$
kT	keV	-	-	-	-	-	$0.831^{+0.03}_{-0.05}$
$N_{\rm diskbb}$	-	-	-	-	-	-	1649^{+76}_{-49}
$f_{\rm refl}$	-	$0.249^{+0.005}_{-0.007}$	$0.22^{+0.02}_{-0.02}$	$0.228^{+0.017}_{-0.011}$	0.26 ± 0.02	$0.195^{+0.012}_{-0.030}$	$1.45^{+0.06}_{-0.03}$
$\log(F_{\rm dis})$	$\rm erg\,cm^{-2}\,s^{-1}$	$-11.00^{+0.10}_{-0.12}$	$-10.73^{+0.02}_{-0.13}$	-10.62 ± 0.08	$-10.50^{+0.09}_{-0.08}$	$-1.06^{+0.08}_{-0.13}$	<-10.89
C-stat/ν							1048.68/971
$L_{0.1-100\rm keV}/L_{\rm Edd}$	%	1.2	2.0	3.1	4.0	0.7	26.7

compared to LF observations. In this section, we discuss the spectral fitting results by comparing with previous data analysis and accretion disc theories.

4.1 Comparison with previous results

First, the most significant difference from previous results is the close-to-solar disc iron abundance. Previously, Parker

et al. (2016); Wang-Ji et al. (2018) obtained a disc iron abundance of $Z_{\rm Fe} = 6.6^{+0.5}_{-0.6}Z_\odot$ and $Z_{\rm Fe} \approx 8Z_\odot$ respectively by analysing the same spectra considered in this work. Similar result was achieved by Fürst et al. (2015). A high iron abundance of $Z_{\rm Fe} = 5 \pm 1Z_\odot$ was also found by analysing stacked *RXTE* spectra (García et al. 2015). All of their work was based on the assumption for a fixed disc density $n_{\rm e} = 10^{15}\,\rm cm^{-3}$. By allowing the disc density $n_{\rm e}$ to vary as a
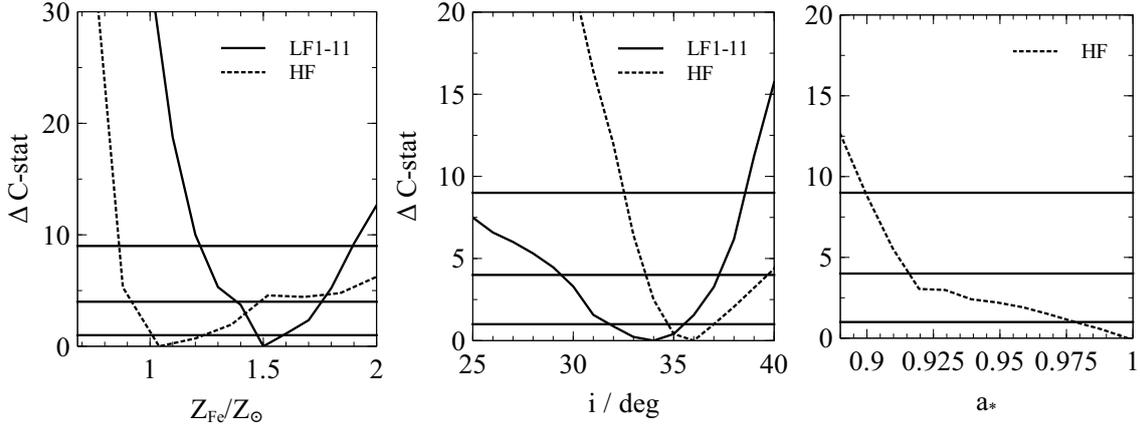
Figure 7. C-stat contour plots for the disc iron abundance and the relativistic reflection parameters obtained by fitting LF 1-11 spectra simultaneously (solid lines) and only the HF spectra (dashed line). The solid lines show the 1σ, 2σ, and 3σ ranges.

free parameter during spectral fitting, we obtained a close-to-solar disc iron abundance ($Z_{Fe} = 1.50^{+0.12}_{-0.04}Z_\odot$ for LF observations and $Z_{Fe} = 1.05^{+0.17}_{-0.15}Z_\odot$ for HF observations). The best-fit disc iron abundance for the LF spectra is slightly higher than the value for the HF spectra at 90% confidence. However they are consistent within 2σ confidence range. See the left panel of Fig. 7 for the constraints on the disc iron abundance parameter. A similar conclusion was achieved by analysing the intermediate flux state spectra of Cyg X-1 (Tomsick et al. 2018) with variable density reflection model. However a fixed solar iron abundance was assumed in their modelling.

Second, the best-fit disc viewing angle measured for GX 339-4 is different in different works. The middle panel of Fig. 7 shows the constraint of the disc viewing angle given by multi-epoch LF spectral analysis and HF spectral analysis. The two measurements are consistent at the 90% confidence level ($i = 34 \pm 2$ deg for the LF observations and $i = 35.9^{+1.6}_{-2.0}$ deg for the HF observations). Although our best-fit value is lower compared with the measurement in Wang-Ji et al. (2018) ($i = 40°$) and higher than the measurement in Parker et al. (2016) ($i = 30°$), all the previous reflection based measurements are consistent with our results at 2σ level. Similarly Tomsick et al. (2018) measured a different viewing angle for Cyg X-1 compared with previous works. It indicates that a slightly different viewing angle measurement might be common when allowing the disc density n_e to vary as a free parameter during the spectral fitting.

Third, a high black hole spin ($a_* > 0.93$) is given by the disc reflection modelling in the HF spectral analysis. Due to the lack of precise measurement of the source distance and the central black hole mass, we can only give a rough estimation of the inner radius through the normalization of the diskbb component in the HF observations. The normalization parameter is defined as $N_{diskbb} = (r_{in}/D_{10kpc})^2 \cos i$, where the D_{10kpc} is the source distance in units of 10 kpc and i is the disc viewing angle. The best-fit value is $N_{diskbb} = 1649^{+76}_{-49}$, corresponding to an inner radius of $r_{in} \approx 45$ km $\approx 3r_g$ assuming $M_{BH} = 10M_\odot$ and $D = 10$ kpc. We also fitted the thermal component with kerrbb model (Li et al. 2005) as in Parker et al. (2016). kerrbb is a multi-colour blackbody model for a thin disc around a Kerr black hole, which in-

cludes the relativistic effects of spinning black hole. The BH spin and the disc viewing angle are linked to the corresponding parameters in relconv. However we found the source distance and the central black hole mass parameters in kerrbb are not constrained during the spectral fitting. kerrbb model gives a slightly worse fit with ΔC-stat≈ 7 and 2 more free parameters compared to the diskbb model. Since the black hole mass and distance measurement is beyond our purpose, we decide to fit the thermal spectrum in the HF observation with diskbb for simplicity. See Parker et al. (2016) for more discussion concerning the black hole mass and the source distance measurements obtained by fitting with kerrbb. In conclusion, the high spin result in this work is obtained by modelling the relativistic disc reflection component in the HF state of GX 339-4 and consistent with previous reflection-based spectral analysis (e.g. Plant et al. 2015; García et al. 2015; Parker et al. 2016; Wang-Ji et al. 2018). Kolehmainen & Done (2010) found an upper limit of $a_* < 0.9$ by analysing *RXTE* spectra. However they assumed the disc viewing angle is the same as the binary orbital inclination, which is not necessarily the case (e.g. Tomsick et al. 2014; Walton et al. 2016).

Fourth, there is a debate whether the disc is truncated at a significant radius in the brighter phases of the hard state. Compared with the results obtained by modelling the same spectra with $n_e = 10^{15}$cm^{-3} and an additional diskbb component (Wang-Ji et al. 2018), we find larger upper limit of the inner radius in the LF2-5 observations. For example, an upper limit of $r_{in} < 8R_{ISCO}$ is obtained for the LF2 observation, larger than $r_{in} = 1.8^{+3.0}_{-0.6}R_{ISCO}$ found by Wang-Ji et al. (2018). Such difference could be due to different modelling of the disc reflection component. The constraints on the inner radius r_{in} are shown in the top right panel of Fig. 8. Nevertheless, we confirm that the inner radius is not as large as $r_{in} \approx 100r_g$ as proposed by previous analysis (e.g. Plant et al. 2015).

4.2 High density disc reflection

The LF and HF *NuSTAR* and *Swift* spectra of GX 339-4 can be successfully explained by high density disc reflection model with a close-to-solar iron abundance for the disc.
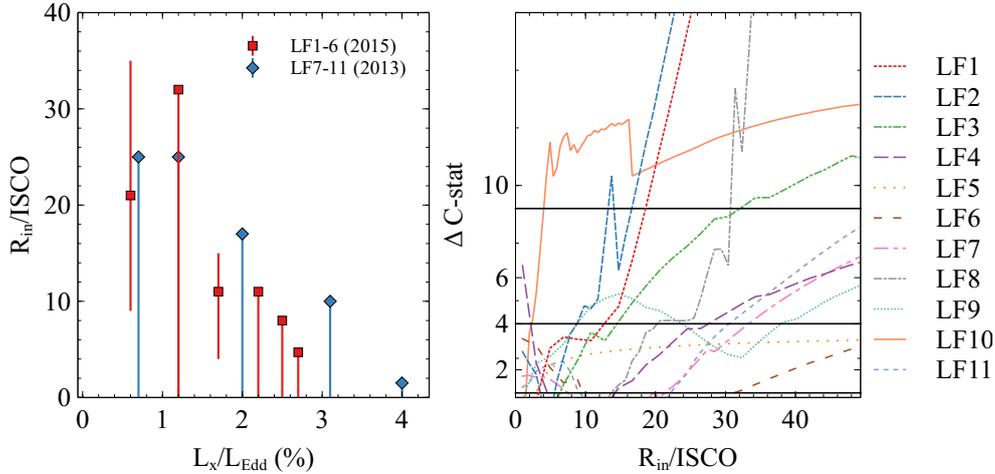
Figure 8. Left: the best-fit inner radius of the disc vs. the X-ray luminosities for LF observations. Red points represent LF1-6 observations and blue points represent LF7-11 observations. The X-ray luminosity L_X is the 0.1–100 keV band Galactic-absorption corrected luminosity calculated using the best-fit model. A black hole mass $M_{BH} = 10 M_\odot$ and a distance d=10 kpc are assumed. The error bars show the 90% confidence ranges of the measurements. See Table 2 for values. Right: the constraints on the inner disc radius for each LF spectra shown in different colours. The solid lines show the 1σ, 2σ, and 3σ ranges.

In the low flux hard states, no additional low-temperature `diskbb` component is required in our modelling. Instead, a quasi-blackbody emission in the soft band of the disc reflection model fits the excess below 2 keV. At higher disc density, the free-free process becomes more important in constraining low energy photons, increasing the disc surface temperature, and thus turning the reflected emission in the soft band into a quasi-blackbody spectrum. See Fig. 5 for a comparison between the best-fit high density reflection model for LF1 observation and a constant disc density model ($n_e = 10^{15}$ cm^{-3}).

In LF states of GX 339-4, a disc density of $n_e \approx 10^{21}$ cm^{-3} is required for the spectral fitting. Our multi-epoch spectral analysis shows tentative evidence that the disc density increases from $\log(n_e/\text{cm}^{-3}) = 20.60^{+0.23}_{-0.12}$ in the highest flux state (LF1) to $\log(n_e/\text{cm}^{-3}) = 21.45^{+0.06}_{-0.13}$ in the lowest flux state (LF6) during the decay of the outburst in 2015, except for LF5 observation. See Table 2 for n_e measurements. Similar pattern can be found in LF7-10 observations. In HF state of GX 339-4, we measure a disc density of $n_e \approx 10^{19}$ cm^{-3} by fitting the broad band spectra with a combination of high density disc model and a multi-colour disc blackbody model. The disc density in HF state is 100 times lower than that in LF states. The 0.1–100 keV band luminosity of GX 339-4 in HF state ($L_X \approx 0.28 L_{Edd}$) is 10 times the same band luminosity in LF states ($L_X = 0.01 - 0.03 L_{Edd}$). While the accretion rate is rather small, the anti-correlation between the disc density and the X-ray luminosity $\log(n_{e1}/n_{e2}) \propto -2\log(L_{X1}/L_{X2})$ is found to agree with the expected behaviour of a standard radiation-pressure dominated disc (e.g. Shakura & Sunyaev 1973; Svensson & Zdziarski 1994). See Section 4.3 for more detailed comparison between the measurements of the disc density and the predictions of the standard disc model.

4.3   Accretion rate and disc density

Svensson & Zdziarski (1994) (hereafter SZ94) reconsidered

the standard accretion disc model (Shakura & Sunyaev 1973, hereafter SS73) by adding one more parameter to the disc energy balance condition - a fraction of the power associated with the angular momentum transport is released from the disc to the corona, denoted as f. Only $1 - f$ of the released accretion power is dissipated in the colder disc itself.

By following SZ94, we can obtain a relation between n_e and f for a radiation-pressure dominated disc:

$$n_e = \frac{1}{\sigma_T R_S} \frac{256\sqrt{2}}{27} \alpha^{-1} R^{3/2} \dot{m}^{-2} [1 - (R_{in}/R)^{1/2}]^{-2} [\xi(1-f)]^{-3}, \quad (1)$$

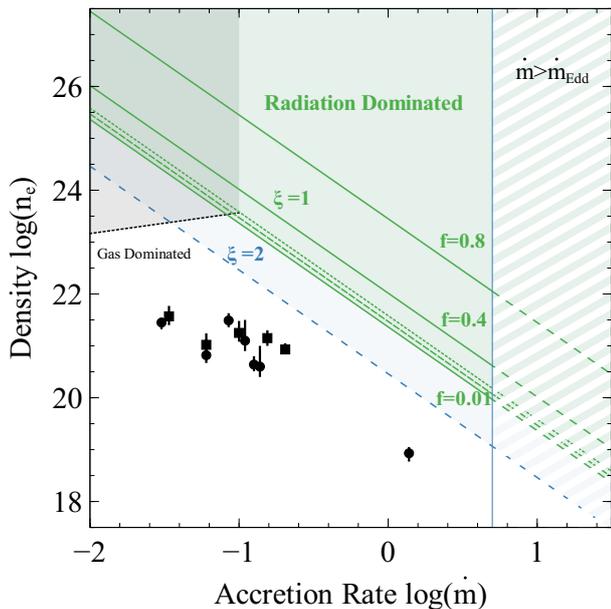where $\sigma_T = 6.64 \times 10^{25}$ cm^2 is the Thomson cross section; R_S is the Schwarzschild radius; R is in the units of R_S; $\dot{m}$ is defined as $\dot{m} = \dot{M}c^2/L_{Edd} = L_{Bol}/\epsilon L_{Edd}$; $L_{Edd} = 4\pi GM m_p c/\sigma_T = 2\pi(m_p/m_e)(m_e c^3/\sigma_T)R_S$ is the Eddington luminosity; ξ is the conversion factor in the radiative diffusion equation and chosen to be 1, 2 or 2/3 by different authors (SZ94). For a radiation-pressure dominated disc, the disc density n_e decreases with increasing accretion rate $\dot{m}$. In Fig. 9, we plot the radiation-pressure dominated disc solutions for $\xi = 1$ in green lines and a solution for $\xi = 2$ in blue.

When $\dot{m} < 0.1$ and f approaches unity, the radiation-pressure dominated radius disappears and gas pressure starts dominates the disc. The relation between n_e and f for a gas-pressure dominated disc is

$$n_e = \frac{1}{\sigma_T R_S} K \alpha^{-7/10} R^{-33/20} \dot{m}^{2/5} [1 - (R_{in}/R)^{1/2}]^{2/5} [\xi(1-f)]^{-3/10},$$

$$(2)$$

where $K = 2^{-7/2}(\frac{512\sqrt{2}\pi^3}{405})^{3/10}(\alpha_f \frac{m_p}{m_e})^{9/10}(\frac{R_S}{r_e})^{3/10}$. α_f is the fine-structure constant; m_p is the proton mass; m_e is the electron mass; r_e is the classical electron radius. An example of a gas-pressure dominated disc solution for $R = 2R_S$ and $f = 0.01$ is shown by the black line in Fig. 9 for comparison. For a gas-pressure dominated disc, the disc density increases with increasing accretion rate.

The best-fit disc density and accretion rate values obtained by fitting GX 339-4 LF1-11 and HF spectra with high

and theoretical predictions in SZ94. Following are possible explanations for the mismatch: 1. the disc density shown in Eq. 1 is assumed to be constant throughout the vertical profile of the disc (SS73). The n_e parameter we measure using reflection spectroscopy is however the surface disc density within a small optical depth (Ross & Fabian 2007). For example, three-dimensional MHD simulations show that the vertical structure of radiation-pressure dominated disc density is centrally concentrated (e.g. Turner 2004; Hirose et al. 2006). 2. the accretion rate might be underestimated by assuming $L_{Bol} \approx L_{0.1-100\text{keV}}$, although we do not expect other bands of GX 339-4 to make a large contribution to its bolometric luminosity; 3. there is a large uncertainty on the black hole mass, the disc accretion efficiency, and the source distance measurements for GX 339-4. For example, the most recent near-infrared study shows that the central black hole mass in GX 339-4 could be within $2 - 10 M_\odot$ (Heida et al. 2017). Nevertheless, the use of the high density reflection model enables us to estimate the density of the disc surface in different flux states of an XRB and an anti-correlation between n_e and L_X has been found in GX 339-4.

4.4 Future work

In our work, we conclude that the high density reflection model can explain both the LF and HF spectra of GX 339-4 with a close to solar iron abundance. No additional black-body component is statically required during the spectral fitting of the LF states. On one hand, the strong degeneracy between the `diskbb` component and the absorber column density is due to the low S/N of the *Swift* XRT observations. More pile-up free soft band spectra are required to obtain a more detailed spectral shape at the extremely LF state of GX 339-4, such as from *NICER*. On the other hand, more detailed spectral modelling is required. For example, a more physics model, such as Comptonization model, is required for the coronal emission modelling in the broad band spectral analysis. The disc thermal photons from the disc to the reflection layer need to be taken into account in future reflection modelling, especially in the XRB soft states where a strong thermal spectrum is shown.

Figure 9. Disc density $\log(n_e/\text{cm}^{-3})$ vs. accretion rate $\log(\dot{m})$ based on the radiation-pressure dominated (green) and gas-pressure dominated (black) disc solutions in SZ94, assuming $M_{BH} = 10 M_\odot$ and $\alpha = 0.1$. The solid green lines show the solutions with different coronal power fraction f at $R = 2R_S$. The dashed and dotted green lines show the radiation pressure-dominated solution with $f = 0.01$ at $R = 6, 8R_S$ respectively. The black circular points show the surface disc density and the mass accretion rate measurements of GX 339-4 in LF and HF states in 2015 and the black squares show the measurements for observations in 2013. The mass accretion rate is estimated using $\dot{m} = L_{Bol}/\epsilon L_{Edd} \approx L_{0.1-100\text{keV}}/\epsilon L_{Edd}$ in this work. A Novikov-Thorne accretion efficiency $\epsilon = 0.2$ (Novikov & Thorne 1973; Agol & Krolik 2000) and an inner disc radius of $R_{in} = 1R_S$ is assumed for a spinning black hole with $a_* = 0.95$. The black vertical line shows the Eddington accretion limit $\dot{m}_{Edd} = 1/\epsilon \approx 5$. $\xi = 1$ is assumed during the calculation as in SZ94. The blue solid line is shown for the radiation-pressure dominated disc solution with $R = 2R_S$ and $f = 0.01$, assuming $\xi = 2$.

density reflection model are shown by black points in Fig. 9. The accretion rate is calculated using $\dot{m} = L_{Bol}/\epsilon L_{Edd} \approx L_{0.1-100\text{keV}}/\epsilon L_{Edd}$, where ϵ is the accretion efficiency and $L_{0.1-100\text{keV}}$ is the 0.1–100keV band absorption corrected luminosity calculated using the best-fit model. According to Novikov & Thorne (1973); Agol & Krolik (2000), an accretion efficiency of $\epsilon = 20\%$ is assumed for a spinning black hole with $a_* = 0.95$ measured in Section 3.2. A black hole mass of $10 M_\odot$ and a source distance of $10 \, \text{kpc}$ are assumed.

The 0.1–100 keV band luminosity in the HF state of GX 339-4 is approximately 10 times the same band luminosity in the LF states. The disc density in the HF state is 2 orders of magnitude lower than the density in the LF1-6 states. The anti-correlation between its density and accretion rate is expected according to the radiation-pressure dominated disc solution in SZ94 ($\log(n_e) \propto -2\log(\dot{m})$, as in Eq. 1). However the disc density measurements for GX 339-4 are lower than the predicted values for corresponding accretion rates. See Fig. 9 for comparison between measurements

REFERENCES

Agol E., Krolik J. H., 2000, ApJ, 528, 161

Arnaud K. A., 1996, XSPEC: The First Ten Years

Barr P., White N. E., Page C. G., 1985, Monthly Notices of the Royal Astronomical Society, 216, 65P

Chiang C.-Y., Walton D. J., Fabian A. C., Wilkins D. R., Gallo L. C., 2015, MNRAS, 446, 759

Dauser T., Garcia J., Wilms J., Böck M., Brenneman L. W., Falanga M., Fukumura K., Reynolds C. S., 2013, MNRAS, 430, 1694

Dauser T., García J., Walton D. J., Eikmann W., Kallman T., McClintock J., Wilms J., 2016, A&A, 590, A76

Esin A. A., McClintock J. E., Narayan R., 1997, ApJ, 489, 865

Fabian A. C., et al., 2009, Nature, 459, 540

Fürst F., et al., 2015, ApJ, 808, 122

García J., Kallman T. R., 2010, ApJ, 718, 695

García J. A., Steiner J. F., McClintock J. E., Remillard R. A., Grinberg V., Dauser T., 2015, ApJ, 813, 84

García J. A., Fabian A. C., Kallman T. R., Dauser T., Parker M. L., McClintock J. E., Steiner J. F., Wilms J., 2016, MN-RAS, 462, 751

George I. M., Fabian A. C., 1991, MNRAS, 249, 352

Gou L., et al., 2014, ApJ, 790, 29

Grupe D., Komossa S., Leighly K. M., Page K. L., 2010, ApJS, 187, 64

Heida M., Jonker P. G., Torres M. A. P., Chiavassa A., 2017, ApJ, 846, 132

Hirose S., Krolik J. H., Stone J. M., 2006, ApJ, 640, 901

Hynes R. I., Steeghs D., Casares J., Charles P. A., O'Brien K., 2003a, ApJ, 583, L95

Hynes R. I., Steeghs D., Casares J., Charles P. A., O'Brien K., 2003b, ApJ, 583, L95

Jiang J., et al., 2018, MNRAS, 477, 3711

Kalberla P. M. W., Burton W. B., Hartmann D., Arnal E. M., Bajaja E., Morras R., Pöppel W. G. L., 2005, A&A, 440, 775

Kerr R. P., 1963, Phys. Rev. Lett., 11, 237

Kolehmainen M., Done C., 2010, Monthly Notices of the Royal Astronomical Society, 406, 2206

Li L.-X., Zimmerman E. R., Narayan R., McClintock J. E., 2005, ApJS, 157, 335

Matsuoka M., et al., 2009, PASJ, 61, 999

Miller J. M., et al., 2004, ApJ, 606, L131

Miller J. M., Homan J., Steeghs D., Rupen M., Hunstead R. W., Wijnands R., Charles P. A., Fabian A. C., 2006, ApJ, 653, 525

Miller J. M., et al., 2008, ApJ, 679, L113

Morrison R., McCammon D., 1983, ApJ, 270, 119

Muñoz-Darias T., Casares J., Martínez-Pais I. G., 2008, MNRAS, 385, 2205

Narayan R., 2005, Ap&SS, 300, 177

Narayan R., McClintock J. E., 2008, New Astron. Rev., 51, 733

Novikov I. D., Thorne K. S., 1973, in Dewitt C., Dewitt B. S., eds, Black Holes (Les Astres Occlus). pp 343–450

Oda M., Gorenstein P., Gursky H., Kellogg E., Schreier E., Tananbaum H., Giacconi R., 1971, ApJ, 166, L1

Parker M. L., et al., 2014, MNRAS, 443, 1723

Parker M. L., et al., 2015, ApJ, 808, 9

Parker M. L., et al., 2016, ApJ, 821, L6

Parker M. L., Miller J. M., Fabian A. C., 2018, MNRAS, 474, 1538

Plant D. S., Fender, R. P. Ponti, G. Muñoz-Darias, T. Coriat, M. 2015, A&A, 573, A120

Reis R. C., Fabian A. C., Ross R. R., Miniutti G., Miller J. M., Reynolds C., 2008, MNRAS, 387, 1489

Reis R. C., Miller J. M., Reynolds M. T., Fabian A. C., Walton D. J., Cackett E., Steiner J. F., 2013, ApJ, 763, 48

Reynolds C. S., Nowak M. A., 2003, Phys. Rep., 377, 389

Reynolds C. S., Brenneman L. W., Lohfink A. M., Trippe M. L., Miller J. M., Fabian A. C., Nowak M. A., 2012, ApJ, 755, 88

Ross R. R., Fabian A. C., 2005, MNRAS, 358, 211

Ross R. R., Fabian A. C., 2007, MNRAS, 381, 1697

Shakura N. I., Sunyaev R. A., 1973, A&A, 24, 337

Steiner J. F., McClintock J. E., Remillard R. A., Gou L., Yamada S., Narayan R., 2010, ApJ, 718, L117

Svensson R., Zdziarski A. A., 1994, ApJ, 436, 599

Tanaka Y., et al., 1995, Nature, 375, 659

Tomsick J. A., Yamaoka K., Corbel S., Kaaret P., Kalemci E., Migliari S., 2009, ApJ, 707, L87

Tomsick J. A., et al., 2014, ApJ, 780, 78

Tomsick J. A., et al., 2018, ApJ, 855, 3

Turner N. J., 2004, ApJ, 605, L45

Walton D. J., et al., 2016, ApJ, 826, 87

Walton D. J., et al., 2017, ApJ, 839, 110

Wang-Ji J., et al., 2018, ApJ, 855, 61

Wang H., Zhou H., Yuan W., Wang T., 2012, ApJ, 751, L23

Willingale R., Starling R. L. C., Beardmore A. P., Tanvir N. R., O'Brien P. T., 2013, MNRAS, 431, 394

Wilms J., Allen A., McCray R., 2000, ApJ, 542, 914

Zdziarski A. A., Gierliński M., Mikołajewska J., Wardziński G., Smith D. M., Harmon B. A., Kitamoto S., 2004, MNRAS, 351, 791

This paper has been typeset from a T_EX/L^AT_EX file prepared by the author.